

1 **Mixed layer depth seasonality modulates summertime**  
2 **SST variability in the Southern Ocean**

3 **Earle A. Wilson<sup>1</sup>, David B. Bonan<sup>1</sup>, Andrew F. Thompson<sup>1</sup>, Natalie**  
4 **Armstrong<sup>2</sup>, Stephen C. Riser<sup>3</sup>**

5 <sup>1</sup>Environmental Science and Engineering, California Institute of Technology, Pasadena, CA, USA

6 <sup>2</sup>Department of Environmental Health and Engineering, Johns Hopkins University, Baltimore, MD, USA

7 <sup>3</sup>School of Oceanography, University of Washington, Seattle, WA, USA

8 **Key Points:**

- 9
- 10 • During the austral spring of 2016 and 2019, the Southern Ocean experienced unprece-
  - 11 dented near-circumpolar surface warming events.
  - 12 • Both warming events were initiated by a weakening of the circumpolar westerlies,
  - 13 which led to unusually rapid seasonal shoaling and warming of the mixed layer.
  - 14 • The seasonal phasing of the mixed layer shoaling and warming extremes are linked
- to interannual variability of the Southern Annular Mode.

---

Corresponding author: Earle Wilson, [earlew@caltech.edu](mailto:earlew@caltech.edu)

## Abstract

In recent years, the Southern Ocean has experienced unprecedented surface warming and sea ice loss—a stark reversal of sea ice expansion and surface cooling trends that prevailed over preceding decades. The most dramatic changes occurred in the austral spring of 2016 when Antarctic sea-ice extent (SIE) reached a record minimum as sea surface temperatures (SST) climbed to a near-record high. In late 2019, another circumpolar surface warming event spanned the Southern Ocean, albeit with no appreciable decline in Antarctic SIE. A mixed layer heat budget analysis reveals that these recent circumpolar surface warming events were triggered by a strong weakening of the circumpolar westerlies, which decreased northward Ekman transport and accelerated the seasonal shoaling of the mixed layer. The latter effect amplified the surface warming effect of air-sea heat fluxes during months of peak solar insolation. The late 2016 and 2019 circumpolar warming events occurred when the Southern Annular Mode (SAM) was in a strongly negative phase, and examination of the CESM1 large ensemble suggests that these events fall within the envelope of internal variability. This analysis demonstrates that the seasonal phasing of mixed layer depth shoaling and surface heat fluxes is a significant driver of interannual variability in Southern Ocean summertime SST. Projections of summertime SST in the Southern Ocean will hinge on accurate representations of surface wind variability and mixed layer depth seasonality.

## Plain Language Summary

This study examines the physical mechanisms responsible for recent surface warming anomalies in the Southern Ocean, specifically the abrupt circumpolar surface warming events of late 2016 and 2019. These unprecedented surface warming anomalies were triggered by a weakening of the circumpolar westerlies, which decreased the northward transport of cold surface waters across the Southern Ocean and reduced the depth of the surface mixed layer. The latter effect caused more heat to be trapped near the surface, leading to record-high sea surface temperatures. These surface warming anomalies are linked to internal climate variability associated with the Southern Annual Mode.

## 1 Introduction

The Southern Ocean has experienced exceptional sea ice decline and surface warming in recent years (Figure 1). During the austral spring of 2016, Antarctic sea ice retreated at an unusually rapid rate before reaching a record-low extent the following summer (Turner

46 et al., 2017; Parkinson, 2019; Eayrs et al., 2021). This anomalous sea ice decline coincided  
47 with widespread surface warming that extended beyond the Antarctic sea ice zone and  
48 culminated in record-high summertime sea surface temperatures (SSTs) (Stuecker et al.,  
49 2017; Meehl et al., 2019, Figure 1a). While Southern Ocean SSTs returned to normal after  
50 a few months, Antarctic sea-ice extent (SIE) remained exceptionally low over the next three  
51 years. In late 2019, the Southern Ocean experienced another abrupt circumpolar surface  
52 warming event of similar magnitude and spatial extent as the anomalous warming of late  
53 2016 (Figure 1b).

54 The extent to which these recent warming and sea ice loss anomalies reflect a shift in the  
55 Southern Ocean climate or transient manifestations of internal variability remains unclear.  
56 Over the preceding decades, the Southern Ocean experienced robust sea ice expansion and  
57 surface cooling that were near circumpolar in extent (Yuan & Martinson, 2000; Cavalieri et  
58 al., 2003; Simmonds, 2015). The underlying drivers responsible for these longer timescale  
59 trends are uncertain; possible mechanisms include the strengthening of the circumpolar  
60 westerlies (Fan et al., 2014; Kostov et al., 2017), increases in surface freshwater fluxes and  
61 stratification (Bintanja et al., 2013; Purich et al., 2018; Haumann et al., 2020), atmospheric  
62 teleconnections from the tropical Pacific (Meehl et al., 2016; Li et al., 2021; Chung et al.,  
63 2022), and internal climate variability associated with Weddell Sea deep convection (Zhang  
64 et al., 2019). While it is certain that ongoing greenhouse emissions will eventually lead  
65 to sustained warming and sea ice loss across the Southern Ocean (Ferreira et al., 2015;  
66 Armour et al., 2016; Kostov et al., 2017), the timescale over which an anthropogenic signal  
67 will emerge above internal variability is poorly constrained (Doddridge et al., 2019; Rackow  
68 et al., 2022).

69 Previous studies suggest that the anomalous decline in Antarctic SIE that began in  
70 2016 was due to multiple mechanisms operating over various timescales. This sea ice loss  
71 event has been linked to anomalous variations in the Southern Annular Mode (SAM), El  
72 Niño–Southern Oscillation (ENSO), and Indian Ocean Dipole (IOD), which collectively  
73 weakened the circumpolar westerly jet and facilitated anomalous poleward advection of  
74 warm subtropical air into the subpolar region (Stuecker et al., 2017; Schlosser et al., 2018;  
75 Wang et al., 2019; Purich & England, 2019). These mechanisms are distinct from the slower  
76 process of enhanced upwelling of warm Circumpolar Deep Water (CDW) that is expected  
77 to drive Southern Ocean sea ice loss and surface warming over the next century (Bitz &  
78 Polvani, 2012; Ferreira et al., 2015). However, there is evidence that the gradual build-up

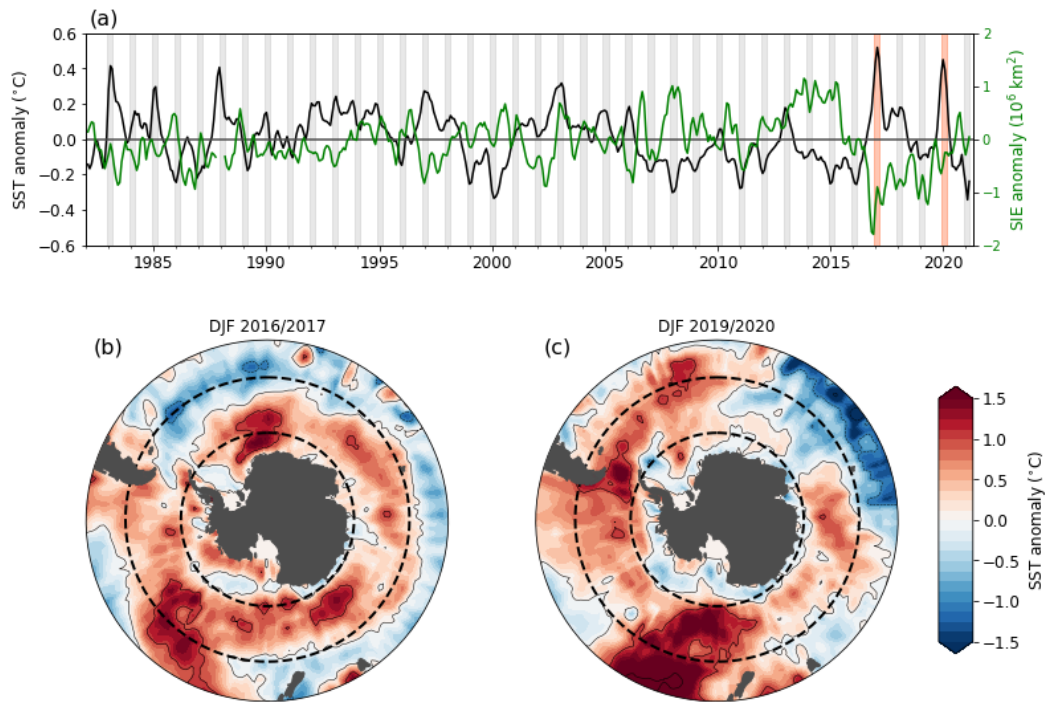


**Figure 1.** (a) Temporal evolution of anomalous SST (black) and Antarctic SIE (green) in the Southern Ocean. (b, c) Seasonally averaged maps of anomalous SST during December–February (DJF) of 2016/2017 and 2019/2020. In (a), the vertical gray bars highlight austral summer (December–February). Dashed lines in (b) and (c) highlight 50°S–65°S, the latitudes over which the SST anomalies are spatially averaged in (a). Each time series has been smoothed with a 3-month rolling average.

79 of subsurface heat in the seasonal sea ice zone may have preconditioned some areas of the  
80 Southern Ocean for an unusually rapid springtime retreat of Antarctic sea ice (Meehl et al.,  
81 2019; Campbell et al., 2019).

82 It is likely that the mechanisms responsible for the recent decline in Antarctic sea ice are  
83 related but distinct from those that led to the recent circumpolar surface warming events.  
84 Though the 2016 surface warming coincided with a steep loss in Antarctic sea ice, this was  
85 not the case in late 2019 (Figure 1a). Furthermore, previous circumpolar surface warming  
86 events, such as those that occurred during the austral spring and summers of 1982/1983  
87 and 1987/1988, were not accompanied by an appreciable decrease in Antarctic SIE (Figure  
88 1a). As with the late 2016 and 2019 warming events, other prominent circumpolar warming  
89 events extended beyond the seasonal sea ice zone. Though previous studies have established  
90 links between Southern Ocean SST anomalies and the variance of SAM and ENSO (Sen  
91 Gupta & England, 2006; Sallée et al., 2010; Ciasto & England, 2011; Ding et al., 2012), there  
92 is no clear relationship between the intensity of SAM or ENSO phases and the magnitude of  
93 Southern Ocean SST anomalies. Thus, the particular set of circumstances that facilitated  
94 the extraordinary summertime SST anomalies in 2016/2017 and 2019/2020 remain unclear.  
95 Since these surface warming events occur in spring and summer, they also provide a glimpse  
96 of the maximum SSTs that may occur across the Southern Ocean. Critically, circumpolar  
97 warming events may provide the basis for marine heatwaves (MHWs), more localized SST  
98 extremes that can lead to sharp declines in biodiversity and the collapse of ecosystems  
99 (Hobday et al., 2016; Frölicher et al., 2018; Holbrook et al., 2019; Smale et al., 2019; Oliver  
100 et al., 2021). Therefore, understanding the mechanisms that may lead to surface warming  
101 extremes is an essential step toward characterizing and predicting ecological sustainability  
102 in the Southern Ocean.

103 The primary purpose of this work is to elucidate the large-scale atmospheric and oceanic  
104 processes that give rise to extreme and abrupt circumpolar surface warming across the  
105 Southern Ocean. This work builds on previous analyses that have examined the seasonal  
106 evolution of Southern Ocean mixed layer temperature (MLT) (Dong et al., 2007, 2008;  
107 Tamsitt et al., 2016; Pellichero et al., 2017) by focusing on processes that can lead to  
108 severe surface warming. Likewise, our analysis extends previous work that has explored  
109 the Southern Ocean response to SAM and ENSO (Sen Gupta & England, 2006; Sallée et  
110 al., 2010; Ciasto & England, 2011) by explicitly examining how the seasonal phasing of  
111 these modes of climate variability can produce extreme summertime SSTs. In doing so, we

112 assess the extent to which recent circumpolar surface warming anomalies can be explained  
113 by internal variability. A key result of this analysis is that variations in the seasonal phasing  
114 of mixed layer depth (MLD) and solar insolation during austral spring are a major source  
115 of interannual variability in Southern Ocean summertime SST. In particular, a sustained  
116 period of negative SAM in late austral spring, similar to what occurred in late 2016 and  
117 2019, provides favorable conditions for abrupt and widespread surface warming anomalies  
118 across the Southern Ocean.

## 119 **2 Data and Methods**

### 120 **2.1 Observations and reanalyses**

121 Monthly SST data were obtained from the NOAA Optimum Interpolation (OI) SST V2  
122 product (Reynolds et al., 2002), while subsurface temperature and salinity variability are  
123 assessed from the Argo-based Roemmich-Gilson climatology (Roemmich & Gilson, 2009).  
124 Estimates of Antarctic sea ice concentration (SIC) were retrieved from the NOAA/NSIDC  
125 Climate Data Record (CDR) of SIC (Meier et al., 2013). SIE is defined as the area over which  
126 SIC is greater than 15%. Estimates of surface wind stress, sea level pressure, and air-sea  
127 heat fluxes were sourced from the ECMWF monthly ERA5 global atmospheric reanalysis  
128 (Hersbach et al., 2020). The reanalysis estimates were regridded from a  $0.25^\circ$  by  $0.25^\circ$   
129 horizontal grid to a coarser  $1^\circ$  by  $1^\circ$  horizontal grid using a bi-linear interpolation scheme,  
130 consistent with the RG Argo and the NOAA OI SST data products.

131 While the SST data and atmospheric reanalysis products are analyzed for 1982–2020,  
132 the mixed layer heat budget analysis is carried out for the 2004–2020 period when subsurface  
133 Argo data are available. The depth of the mixed layer is defined using a density threshold of  
134  $0.03 \text{ kg m}^{-3}$  (de Boyer Montégut et al., 2004). The SAM index is defined as the zonal-mean  
135 sea level pressure difference between  $65^\circ\text{S}$  and  $40^\circ\text{S}$  (Marshall, 2003). ENSO variability  
136 is quantified using the Niño3.4 metric, which describes the area-averaged SST anomaly  
137 between  $170^\circ\text{W}$ – $120^\circ\text{W}$  and  $5^\circ\text{S}$ – $5^\circ\text{N}$ . The SAM and Niño3.4 indices are normalized by their  
138 respective standard deviations. Anomalies are computed relative to a monthly averaged  
139 climatology. For the SST and reanalysis data, the climatological reference period is 1982–  
140 2015, while for the Argo data, the climatological reference period is 2004–2015.

141 To contextualize recent abrupt circumpolar warming events, observations are compared  
142 with output from the Community Earth System Model Version 1 Large Ensemble (CESM1-

143 LE) (Kay et al., 2015). The CESM1-LE is a state-of-the-art fully coupled,  $1^\circ$  horizontal  
 144 resolution 40-member initial condition ensemble, where each ensemble member is subjected  
 145 to identical historical and RCP8.5 external forcing scenarios. Each member differs slightly  
 146 in the initial atmospheric state, producing a representation of internal variability across  
 147 ensemble members, in the presence of forced climate change. We focus on the 1980–2020  
 148 period that overlaps with the modern satellite record.

## 149 2.2 Southern Ocean mixed layer heat budget

150 Physical controls on Southern Ocean SST are evaluated using a mixed layer heat budget.  
 151 In this study, MLT and SST are assumed to be equivalent. The heat budget is constructed  
 152 for the mostly ice-free latitude band of  $50^\circ$ – $65^\circ$ S, which envelops the core of the circumpolar  
 153 westerly jet and much of the Antarctic Circumpolar Current (ACC). Importantly, this is the  
 154 latitudinal band over which zonally averaged SST anomalies are cool (warm) in response  
 155 to a positive (negative) SAM phase (Sen Gupta & England, 2006). Further north, between  
 156  $30^\circ$ S– $50^\circ$ S, the SST response to SAM is reversed. This analysis focuses on the  $50^\circ$ – $65^\circ$ S  
 157 circumpolar band, over which the anomalous warming events of late 2016 and 2019 were  
 158 most apparent.

159 As demonstrated by Dong et al. (2007), domain-averaged variations in MLT  $T_m$  across  
 160 the circumpolar channel is primarily governed by heating due to air-sea fluxes, northward  
 161 Ekman transport, and wind-driven entrainment. This balance is given by

$$162 \frac{1}{A_s} \iint \frac{\partial T_m}{\partial t} dA \approx \frac{1}{A_s} \iint \left( \frac{Q_{ao}}{\rho_0 c_w h_m} - v_{Ek} \frac{\partial T_m}{\partial y} - w_{ent} \frac{\Delta T}{h_m} \right) dA, \quad (1)$$

$$163 \frac{1}{A_s} \iint \dot{T}_m dA \approx \frac{1}{A_s} \iint \left( \dot{T}_{ao} - \dot{T}_{Ek} - \dot{T}_{ent} \right) dA, \quad (2)$$

$$164 \dot{\bar{T}}_m \approx \dot{\bar{T}}_{ao} - \dot{\bar{T}}_{Ek} - \dot{\bar{T}}_{ent}, \quad (3)$$

166 where  $Q_{ao}$  is the net air-sea heat flux comprised of the sum of radiative and turbulent heat  
 167 fluxes,  $v_{Ek}$  is the meridional Ekman velocity,  $\Delta T$  is the temperature difference between the  
 168 mixed layer and just below the mixed layer,  $h_m$  is the mixed layer depth,  $w_{ent} = \dot{h}_m$  is  
 169 the entrainment rate, and  $A_s$  is the surface area of the circumpolar control volume. The  
 170 meridional Ekman velocity is given by  $v_{Ek} = \tau^x / (\rho_0 f h_m)$ , where  $\tau^x$  is the zonal component  
 171 of the surface wind stress,  $\rho_0 = 1025 \text{ kg m}^{-3}$  is a reference seawater density, and  $f \approx 10^{-4}$   
 172  $\text{s}^{-1}$  is the Coriolis parameter. Following the procedure outlined in Dong et al. (2007),  $Q_{ao}$   
 173 is modified slightly to account for the fraction of shortwave radiation that is transmitted  
 174 through the base of the mixed layer.

Equation (3) is valid when evaluating the heat balance over the entire circumpolar channel. Over smaller spatial scales, geostrophic transport and eddy mixing, which are neglected in this framework, have leading-order impacts on surface temperature variability (Tamsitt et al., 2016; du Plessis et al., 2022; Gao et al., 2022). It is also assumed that meridional eddy fluxes across the northern and southern boundaries of the control volume make small contributions to the domain-averaged MLT tendency  $\dot{\bar{T}}_m$  on monthly timescales. Though it is relatively straight-forward to evaluate  $\dot{\bar{T}}_{ao}$  and  $\dot{\bar{T}}_{Ek}$  from Argo data and atmospheric reanalysis,  $T_{ent}$  presents a greater challenge since it is influenced by sub-monthly variations in  $h_m$  that are not well-resolved by the current Argo observing array (Carranza & Gille, 2015). Therefore, the effect of vertical entrainment is estimated from the residual of the other heat budget terms.

### 3 Results

#### 3.1 Climate conditions during recent circumpolar warming events

During the austral spring of 2016 and 2019, the domain-averaged surface buoyancy fluxes across the Southern Ocean were not consistently different from the climatological mean (Figure 2a). Though the late 2016 warming event followed unusually warm winter and spring, this was not the case in 2019. Additionally, the spatial patterns of anomalous air-sea fluxes were not consistent with the patterns of anomalous warming during both circumpolar warming events (Figure 3). While in some instances, patterns of anomalously high air-sea heating and mixed layer warming overlapped, this was often not the case. For example, during October–December of 2019, air-sea heat fluxes across the southern Atlantic favored anomalous surface cooling while the mixed layer warmed at an accelerated rate (Figure 3e,f). Thus, the recent circumpolar warming events cannot be directly attributed to anomalous air-sea heat fluxes.

On the other hand, circumpolar westerlies were extraordinarily weak in late 2016 and 2019, with zonally averaged surface wind stress anomalies exceeding  $-0.04 \text{ N m}^{-2}$  (Figure 2b)—a  $\sim 30\%$  reduction relative to the climatological mean. During both warming events, the collapse of the surface westerlies spanned all longitudes (Figure 3 c, h). Concurrently, there was widespread anomalous MLD shoaling across the Southern Ocean (Figure 3d,f). The anomalous shoaling was most striking in late 2019 when the MLD across the circumpolar channel was, on average, roughly 20% shallower than usual. The late 2016 and 2019

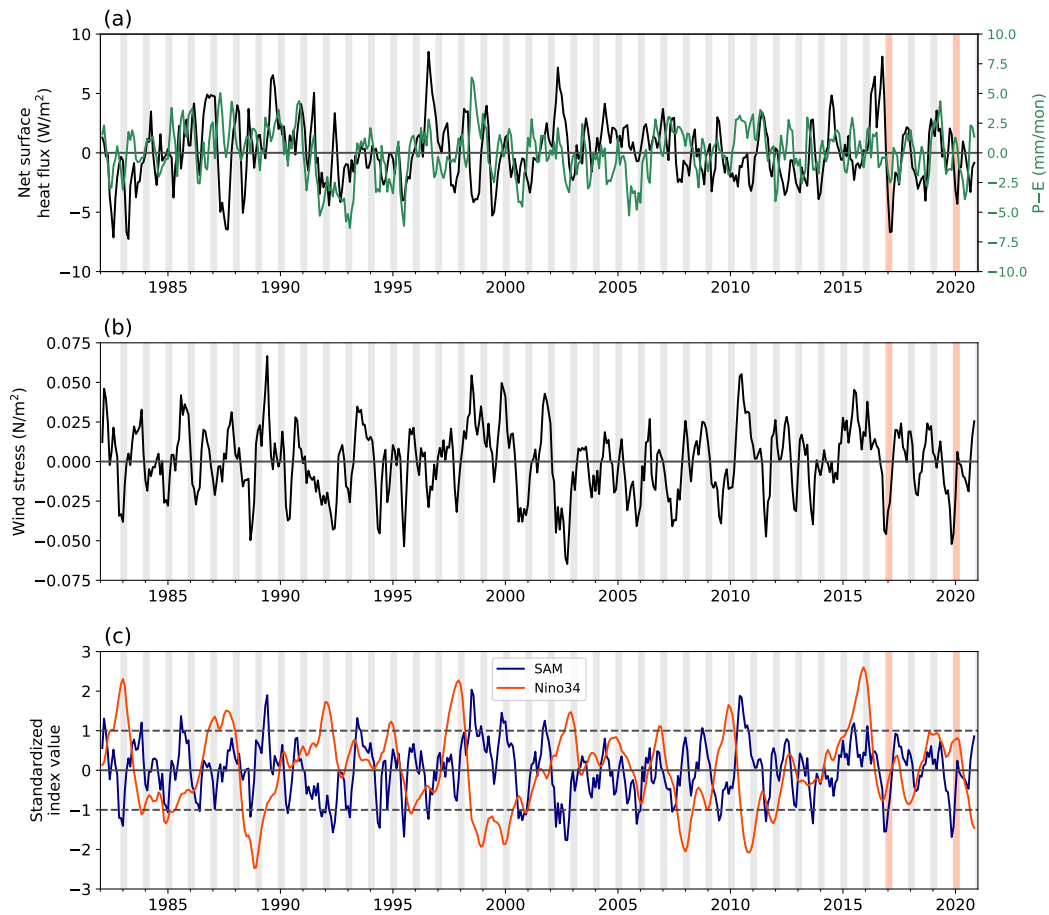


**Figure 2.** (a) Domain-averaged net surface heat flux anomalies (black) and precipitation minus evaporation anomalies ( $P-E$ , green) across  $50^\circ\text{S}$ – $65^\circ\text{S}$ . Positive air-sea heat fluxes signify ocean heat gain. (b) As in (a) but showing zonal wind stress anomalies. (c) Temporal evolution of the SAM (blue) and the Nino3.4 indices (orange). Vertical gray bars highlight austral summer (December–February). The linear trend has been removed from each time series, and temporal variations are smoothed using a 3-month rolling average.

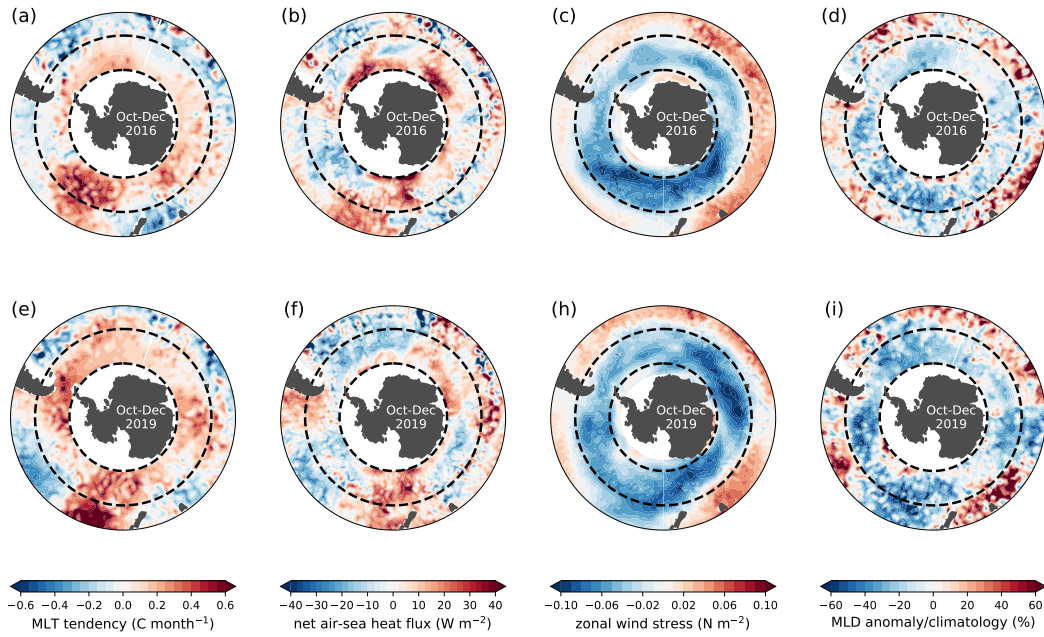


**Figure 3.** Southern Ocean surface conditions during October–December of 2016 (top row) and 2019 (bottom row): (a, e) MLT tendency anomalies, (b, f) Net air-sea heat flux anomalies, (c, h) zonal wind stress anomalies, and (d, i) MLD anomalies as percentages of the monthly climatological means. Black dashed lines outline the circumpolar channel (50°S–65°S over which the mixed layer heat budget is evaluated).

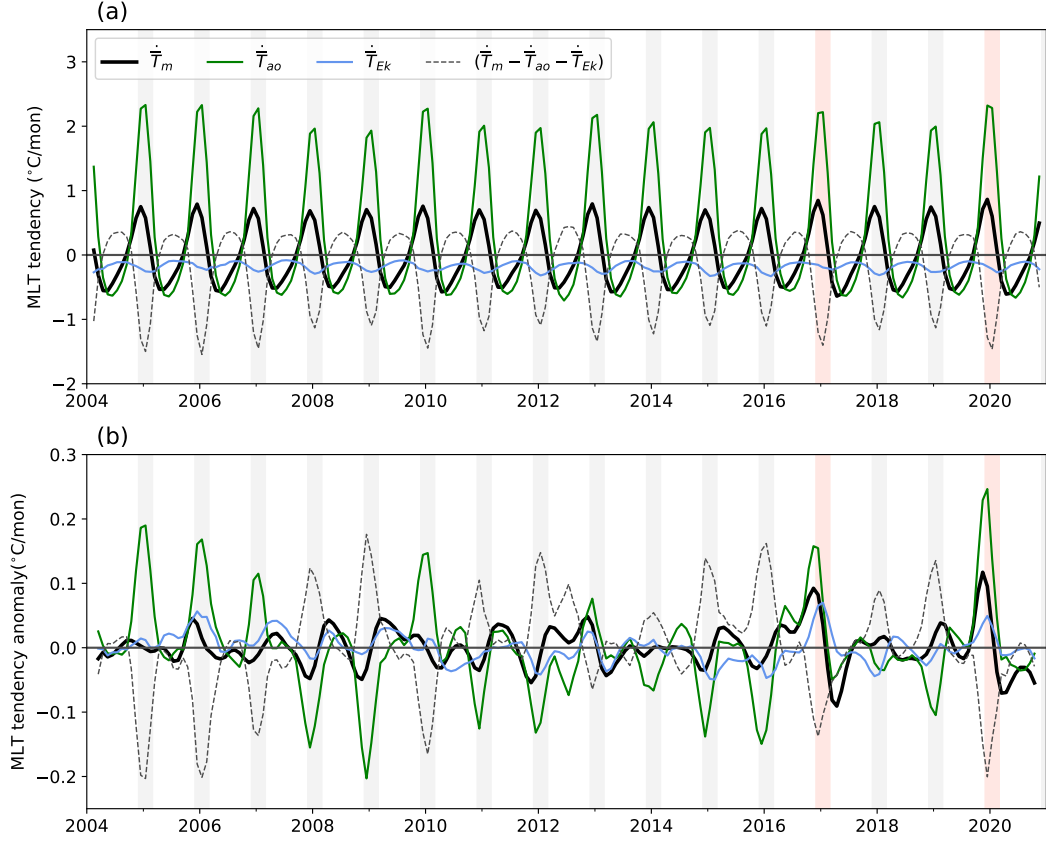


**Figure 4.** Evolution of the Southern Ocean mixed layer heat budget, described by Eq. (3). (a) Monthly tendencies in MLT (black) due to air-sea heat fluxes (green) and meridional Ekman transport (blue). The gray dashed line represents the residual of the heat budget ( $\dot{\bar{T}}_m - \dot{\bar{T}}_{ao} - \dot{\bar{T}}_{Ek}$ ). (b) As in (a) but after removing the monthly climatology. Gray vertical bars highlight December–February.

206 anomalous shoaling events did not coincide with increased surface heat or freshwater fluxes  
 207 (Figure 2a).

208 Consistent with the strong reduction in circumpolar westerly winds, SAM was in an  
 209 exceptionally negative phase during both circumpolar warming events. In both cases, the  
 210 SAM index was roughly 1.5 standard deviations below its annual mean value (Figure 2b).  
 211 ENSO was in a relatively neutral state during these periods, tending towards its La Niña  
 212 and El Niño phases during the austral spring of 2016 and 2019, respectively.

### 213 3.2 Drivers of anomalous mixed layer warming in late 2016 and 2019

214 Evaluating the circumpolar mixed layer heat budget (Equation 3) reveals that the  
 215 heating anomalies associated with air-sea heat fluxes  $\dot{\bar{T}}_{ao}$  and northward Ekman transport  
 216  $\dot{\bar{T}}_{Ek}$  were the primary drivers of the anomalous surface warming in late 2016 and 2019  
 217 (Figure 4). In late 2016,  $\dot{\bar{T}}_{Ek}$  anomalies peaked at roughly  $0.08 \text{ }^\circ\text{C month}^{-1}$ , which was  
 218 slightly less than the overall mixed layer warming of  $0.1 \text{ }^\circ\text{C month}^{-1}$  (Figure 4b). In late  
 219 2019, anomalies in  $\dot{\bar{T}}_{Ek}$  accounted for roughly half of the observed mixed layer warming.  
 220 The decrease in Ekman-driven cooling is consistent with the anomalously weak zonal wind  
 221 stress during these periods (Figure 3c,h). The enhancement of  $\dot{\bar{T}}_{ao}$  was largely due to  
 222 anomalous MLD shoaling. Thus, even though air-sea heat fluxes were not substantially  
 223 different from the climatological mean during the warming events, their effect on MLT was  
 224 greatly amplified.

225 Estimating  $\dot{\bar{T}}_{ent}$  as a residual of Equation (3) suggests that entrainment-driven mixed  
 226 layer cooling was enhanced during late 2016 and 2019 (Figure 4b). This implied amplifica-  
 227 tion of  $\dot{\bar{T}}_{ent}$  under weaker surface winds reveals a complex interplay between wind-driven  
 228 mixing, MLD, and the variance of surface winds. Since  $\dot{\bar{T}}_{ent}$  is dependent on MLD and  
 229 the temperature gradient below the mixed layer (Eq. 3), this term does not necessarily  
 230 scale with the amplitude of the surface wind stress. Moreover, the temperature of a shal-  
 231 lower mixed layer will be more sensitive to the mixing generated by episodic storms and  
 232 strong wind events. Nevertheless, without direct estimates of entrainment-driving mixing,  
 233 the contribution of  $\dot{\bar{T}}_{ent}$  is not well constrained.

### 234 3.3 The seasonal phasing of mixed layer depth and air-sea heat fluxes

235 The seasonal evolution of  $\dot{\bar{T}}_m$  is re-examined in the phase-space defined by  $h_m$  and  
 236  $Q_{ao}$  (Figure 5). Since the seasonal variation of  $\tau^x$  is small compared to that of MLD and  
 237  $Q_{ao}$ , we focus on the sum of the mixed layer warming due to northward Ekman transport  
 238 and air-sea heat fluxes,  $\dot{\bar{T}}_{ao+Ek} \equiv \dot{\bar{T}}_{ao} + \dot{\bar{T}}_{Ek}$ , assuming a constant surface wind stress of  
 239  $\tau^x = 0.15 \text{ N m}^{-2}$ . During the cooling season (March–September),  $\dot{\bar{T}}_{ao}$  and  $\dot{\bar{T}}_{Ek}$  combine to  
 240 cool the relatively deep mixed layer at a peak rate of approximately  $0.75 \text{ }^\circ\text{C month}^{-1}$ . During  
 241 the warming season (October–February),  $\dot{\bar{T}}_{ao+Ek}$  provides a surface warming that reaches  
 242 a maximum of  $\sim 2 \text{ }^\circ\text{C month}^{-1}$  between January and February. The seasonal asymmetry  
 243 of  $\dot{\bar{T}}_{ao+Ek}$  arises from the nonlinear dependence of  $\dot{\bar{T}}_{ao}$  on  $h_m$ . As  $h_m$  approaches its

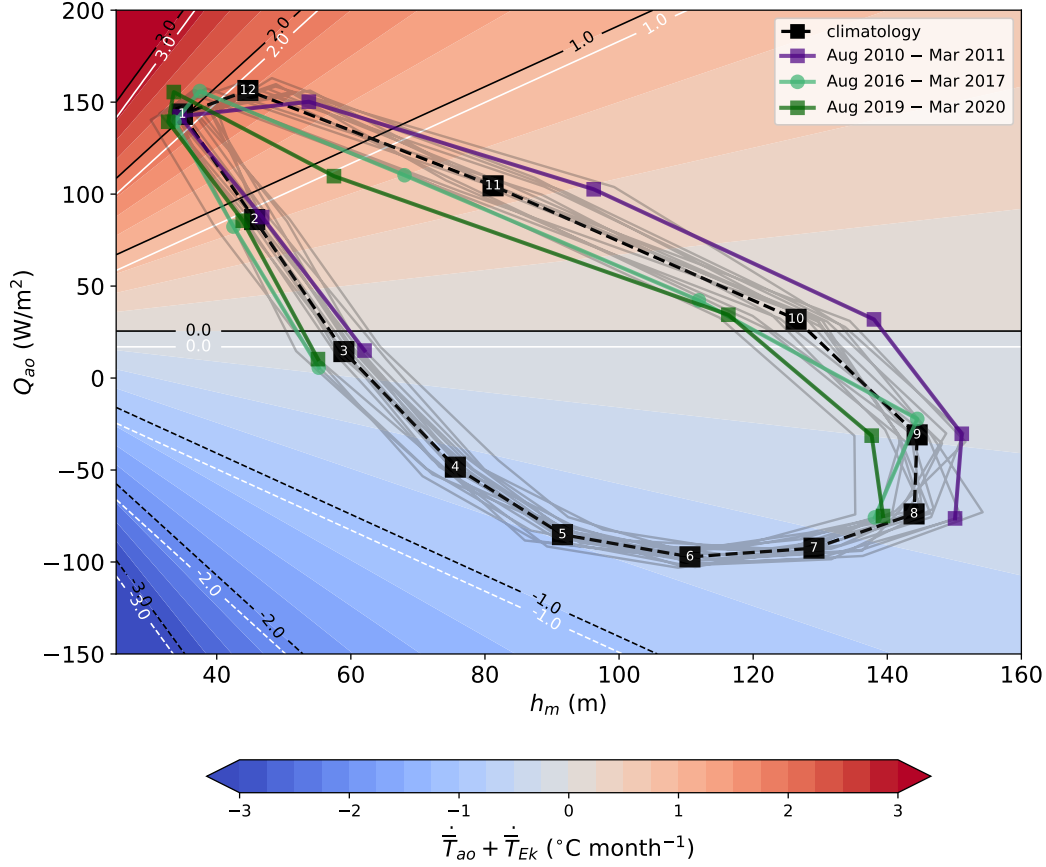


**Figure 5.** Phase diagram showing the relationship between seasonal variations in mixed layer depth  $h_m$ , air-sea heat fluxes  $Q_{ao}$ , and mixed layer temperature tendency due to the sum of air-sea heating  $\dot{T}_{ao}$  and Ekman transport  $\dot{T}_{Ek}$  (contours and shading). Gray lines represent seasonal trajectories from 2004–2020, while the dashed black line represents the climatological mean. For the latter, the numbering of the black squares signifies the calendar month. The purple and green lines highlight trajectories between August–March for 2015/2016, 2016/2017, and 2019/2020, respectively. For the background shading and black contours, the heating associated with northward Ekman transport  $\dot{T}_{Ek}$  is computed assuming a typical value of  $\tau^x = 0.15 \text{ N m}^{-2}$ . White contours show  $\dot{T}_{ao} + \dot{T}_{Ek}$  for the case where  $\tau^x = 0.1 \text{ N m}^{-2}$ .

244 summertime minimum,  $\dot{\bar{T}}_{ao+Ek}$  becomes increasingly sensitive to variations in  $h_m$  and  $Q_{ao}$ ,  
 245 with  $\dot{\bar{T}}_m$  being more sensitive to periods of anomalous mixed layer shoaling than anomalous  
 246 deepening. The effect of  $\dot{\bar{T}}_{Ek}$  may be discerned by the offset in the position of the  $\dot{\bar{T}}_{ao+Ek} = 0$   
 247 contour in Figure 5. In the limit of no surface heating  $Q_{ao} \rightarrow 0$ , only northward Ekman  
 248 transport contributes to heating.

249 In the phase-space defined by  $h_m$  and  $Q_{ao}$ , the impact of the extraordinary MLD  
 250 shoaling in late 2016 and 2019 is immediately evident. During these anomalous warming  
 251 periods (green lines in Figure 5), the Southern Ocean mixed layer followed a relatively  
 252 shallow trajectory in the  $Q_{ao}$ - $h_m$  phase space, which accelerated the springtime warming  
 253 of the mixed layer. In most years,  $Q_{ao}$  reaches a maximum amplitude of  $\sim 150 \text{ W m}^{-2}$   
 254 in December, one month before  $h_m$  reaches its minimum value of  $\sim 40 \text{ m}$ . In late 2016  
 255 and 2019, the seasonal  $h_m$  minimum occurred approximately one month earlier than usual,  
 256 coinciding with maximal air-sea heat fluxes. This shoaling-induced mixed layer warming  
 257 anomaly was most apparent in November of 2019 when  $h_m$  was 20–30 m shallower than  
 258 the climatological mean—a record low for the Argo period. The enhanced mixed layer  
 259 warming due to  $\dot{\bar{T}}_{ao}$  is augmented by a reduction in the cooling provided by  $\dot{\bar{T}}_{Ek}$ , which  
 260 equates to a downward translation of the  $\dot{\bar{T}}_{ao+Ek}$  pattern in Figure 5. The accelerated  
 261 mixed layer warming of late 2016 and 2019, which occurred during strong negative SAM  
 262 events, is contrasted with the more gradual warming that occurred in late 2010 (purple line  
 263 in Figure 5), a period characterized by positive SAM conditions (Figure 2b,c). In the latter  
 264 scenario, the anomalously deep Southern Ocean mixed layer warmed at a relatively slow  
 265 rate, leading to anomalously cool summertime surface temperatures (Figure 1a).

### 266 **3.4 Sensitivity of mixed layer warming to the timing of surface wind anoma-** 267 **lies**

268 The preceding analyses suggest that anomalous mixed layer shoaling and warming dur-  
 269 ing the austral spring of 2016 and 2019 were initiated by a weakening of the circumpolar  
 270 westerlies. To quantify the springtime sensitivity of MLD and MLT to surface wind vari-  
 271 ability, a set of idealized simulations were conducted using a one-dimensional ocean mixing  
 272 model (Appendix A). The Kraus-Turner mixed layer model was forced with idealized sur-  
 273 face fluxes of buoyancy and momentum that mimic observations across  $50^\circ\text{S}$ – $65^\circ\text{S}$  during  
 274 October and February (late spring through summer). For the wind stress forcing, we employ  
 275 synthetic surface winds that are generated from a red-noise spectrum and have a time-mean

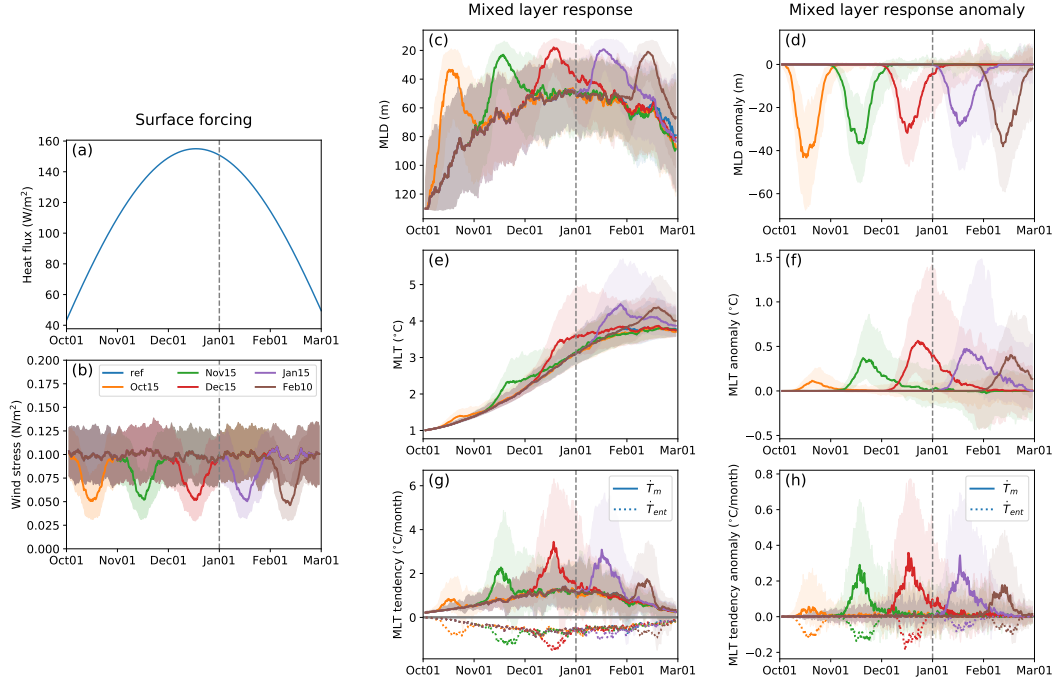


**Figure 6.** Results from the idealized 1D mixing experiments. (a) The prescribed surface heat fluxes used in all experiments. (b) The synthetically generated surface wind stress used in the reference and perturbation experiments, where for the latter set a Gaussian filter was used to dampen the winds by a maximum of 50% over five different periods. Middle column shows the MLD (c), MLT (e) and MLT tendency (g) responses. The right column (d, f, h) shows the mixed layer response anomalies relative to the reference case with no wind perturbation. Each experiment consists of 200 ensemble members forced by a unique wind time series constructed from a red noise spectrum. The shading represents the interquartile range, and solid lines represent the median response. In (g, h), dotted lines represent mixed layer temperature tendency associated with entrainment  $\dot{T}_{ent}$ . The interquartile range for  $\dot{T}_{ent}$  is omitted for clarity. See Section Appendix A for further details.

276 magnitude of  $0.1 \text{ N m}^{-2}$ . For a single experiment, we conducted 200 simulations, each with  
277 a unique surface wind forcing.

278 For the reference case, the mixed layer gradually shoals and warms between October  
279 and February, reaching a minimum depth of roughly 50 m and a maximum temperature of  
280 approximately  $4^\circ\text{C}$ , which are consistent with observations (Figure 6). In the perturbation  
281 experiments, a Gaussian kernel is used to reduce the time-mean wind stress magnitude by  
282 a maximum value of 50% over various 10-day windows. The time-mean wind strength is  
283 reduced during the perturbation period without modifying the temporal variance.

284 Reducing the strength of the winds increases the rate at which the mixed layer shoals  
285 and warms. The amplitude of the MLD shoaling is not sensitive to the timing of the wind  
286 anomaly, with the median response ranging between 30–40 m. In contrast, the amplitude  
287 of mixed layer warming varies substantially with the timing of the wind perturbation. The  
288 median MLT anomaly ranges from  $0.1^\circ\text{C}$  when the wind perturbation is applied in mid-  
289 October to  $0.5^\circ\text{C}$  when the winds are reduced by an equivalent amount in mid-December.  
290 The latter warming anomaly occurs when the MLD and surface heat fluxes are at their  
291 respective minimum and maximum.

292 In the perturbation experiments, weaker winds lead to an increase in entrainment-  
293 driven mixed layer cooling  $\dot{T}_{ent}$ , which is consistent with what is inferred from observations  
294 in late 2016 and 2019 (Figure 4). However, the simulated response of  $\dot{T}_{ent}$  is sensitive to  
295 the temporal variance of the surface winds. In experiments where the temporal variance  
296 is reduced in a similar manner as the temporal mean, the change in  $\dot{T}_{ent}$  is negligible  
297 (not shown). These results indicate that wind-driven entrainment is strongly controlled  
298 by the temporal variance of the wind stress amplitude, with high-wind extremes having a  
299 disproportionate impact on entrainment.

300 Additional simulations (not shown here) were conducted to evaluate the sensitivity of  
301 the mixed layer responses to the duration and sign of the wind perturbation. Prolonging  
302 the weakening of the winds leads to equivalent changes in the MLD and heating tendency  
303 anomalies, with the extended accumulation of  $\dot{T}$  anomalies resulting in a larger absolute  
304 change in MLT. Applying a positive wind perturbation produces a response opposite to the  
305 case with weaker winds, albeit with more minor MLT anomalies due to the deeper mixed  
306 layers.

307            Though idealized, these numerical simulations demonstrate that a reduction in wind-  
308 driven mixing can generate MLT anomalies similar in magnitude to those observed during  
309 the austral spring and summer of 2016/20120 and 2019/2020. The decrease in northward  
310 Ekman transport, a process not included in our idealized model, would further augment the  
311 surface warming response.

### 312            **3.5 Role of internal climate variability**

313            Given the rarity of these abrupt circumpolar warming events and our short observa-  
314 tional record, we examine output from the 40-member CESM1-LE to gain a more robust  
315 understanding of these phenomena. Specifically, we investigate the response of summertime  
316 Southern Ocean SST (December–February; DJF) to variations of SAM in the preceding  
317 austral spring. An observational analysis of the lead-lag relationship between the SAM in-  
318 dex and DJF SST across 50°–65°S shows that maximal correlation ( $r \approx -0.75$ ) is attained  
319 when SST is lagged by one month. Therefore, we assess the relationship between Southern  
320 Ocean SST anomalies in DJF with SAM variability in November–January (NDJ) in the  
321 CESM1-LE. To isolate the effect of internal variability, we evaluate the variance of SAM  
322 and Southern Ocean SST after removing the ensemble-mean values, which represent the  
323 responses to anthropogenic forcing.

324            Though rare, Southern Ocean climate extremes like those observed in late 2016 and  
325 2019 appear in the CESM1-LE (Figure 7a,b). In the CESM1-LE, NDJ periods where the  
326 SAM index is more than 1.5 standard deviations below average occur roughly once every 20  
327 years. The distribution of NDJ SAM events also has a notable skew towards negative SAM  
328 events (Figure 7a). Importantly, the simulated Southern Ocean SST and MLD responses to  
329 late-spring SAM variability are consistent with observations. In particular, the mixed layer  
330 warming and shoaling observed in late 2016 and 2019 are consistent with equivalent events  
331 in the CESM1-LE (Figure 7c, d). To quantify the relative effect of SAM and ENSO in the  
332 CESM1-LE, we create composites of Southern Ocean SST and MLD anomalies using 0.5  
333 standard deviation bins. In the CESM1-LE, strong SAM and ENSO events can occur inde-  
334 pendently, and it is evident that SAM has the dominant control over domain-averaged SST  
335 and MLD anomalies across 50°S–65°S. The sensitivity of summertime Southern Ocean SST  
336 and MLD to SAM variability is less apparent for individual ensemble members, and a strong  
337 dependence on SAM only emerges after averaging anomalies across the 40-member ensem-

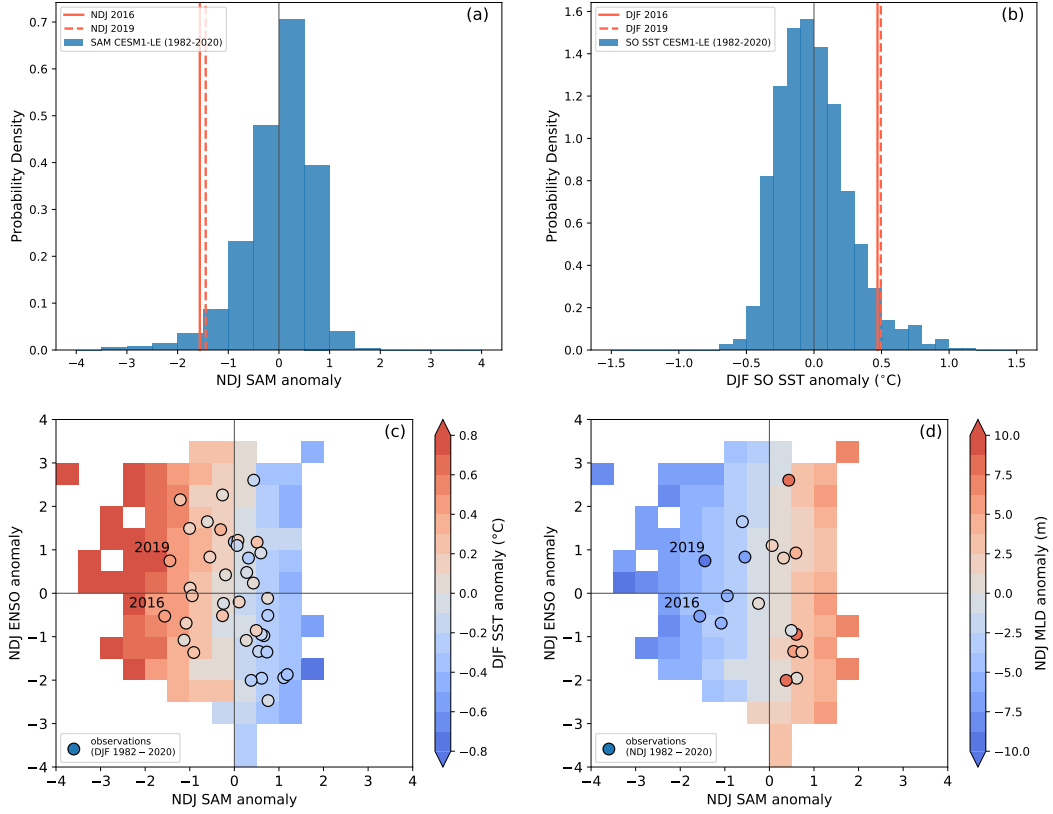


**Figure 7.** Comparisons of SAM and Southern Ocean SST variability in the 40-member CESM1-LE with observations during 1982–2020. (a) Probability density distribution of the November–January (NDJ) SAM index in the CESM1-LE. (b) As in (a), but for domain-averaged DJF Southern Ocean SST anomalies across  $50^{\circ}$ – $65^{\circ}\text{S}$ . (c) Composites of domain-averaged DJF Southern Ocean SST anomalies in relation to NDJ SAM and ENSO. (d) As in (c), but showing NDJ Southern MLD anomalies. For the CESM1-LE results, anomalies refer to deviations from the ensemble mean. In (a) and (b), the frequency distributions of SAM and Southern Ocean SST are generated using 0.5 standard deviations and  $0.1^{\circ}\text{C}$  bins, respectively. For the observed seasonal averages shown here, the listed year represents the year the season begins.

338 ble. These results indicate that other modes of variability significantly impact interannual  
339 variations of Southern Ocean SST and MLD in austral spring.

#### 340 4 Discussion

341 This study demonstrates that the relative seasonal phasing of MLD shoaling and air-sea  
342 heat fluxes is a key driver of interannual variability in summertime Southern Ocean SST.  
343 Between September and December, the zonally averaged MLD between 50°S–65°S shoals  
344 from its winter maximum of  $\sim 150$  m to its summer minimum of  $\sim 50$  m (Fig. 5). The  
345 rate at which this shoaling occurs varies substantially from year to year and produces an  
346 equivalently large spread in the rate at which the mixed layer warms. In the austral spring  
347 of 2016 and 2019, the Southern Ocean mixed layer shoaled at the fastest rates observed  
348 during the Argo era, which amplified the warming effect of solar insolation when it was near  
349 its seasonal maximum. During both events, the anomalous MLD shoaling was initiated by  
350 a dramatic weakening of the circumpolar westerlies associated with strong negative SAM  
351 events. The weaker westerlies also reduced northward Ekman transport, further amplifying  
352 the mixed layer warming.

353 While several studies have shown that SAM has substantial control over springtime  
354 MLD and MLT (e.g., Sen Gupta & England, 2006; Sallée et al., 2010), this study quantifies  
355 the high degree to which mixed layer warming is sensitive to the timing of the SAM anoma-  
356 lies. In particular, a sustained negative SAM event in November is expected to yield surface  
357 warming anomalies that are at least twice that produced by a similar SAM event occurring  
358 one month earlier. The late 2016 and 2019 warming events followed intense periods of neg-  
359 ative SAM, which peaked during November and December, during which the MLT response  
360 to surface wind variability was maximal. This temporal sensitivity may explain why the  
361 negative SAM event in late 2002 did not lead to anomalous surface warming as severe as  
362 what was observed in late 2016 and 2019 (Figs. 1a, 2c). Though the late 2002 negative  
363 SAM event was just as intense and more prolonged than the 2016 and 2019 SAM events,  
364 the former peaked in October before transitioning to a more neutral state in November.

365 Abrupt circumpolar surface warming events, such as those observed across the South-  
366 ern Ocean in late 2016 and 2019, occur in the CESM1-LE. These events are relatively rare,  
367 occurring roughly every 20 years in the CESM1-LE. Additionally, the Southern Ocean SST  
368 and MLD response to SAM in the CESM1-LE aligns well with recent observations. The

369 CESM1-LE also features springtime negative SAM events that are more extreme than what  
370 has been observed over the past four decades, which suggests that the SAM variability  
371 may drive even more intense summertime surface warming anomalies in the future. In the  
372 CESM1-LE, SAM has a much stronger influence on zonally averaged summertime SST vari-  
373 ability across the circumpolar channel than ENSO. However, examining individual ensemble  
374 members reveals that ENSO and other modes of variability can substantially modulate sum-  
375 mertime Southern Ocean SST variability in a given year. Nevertheless, we conclude that  
376 the anomalous circumpolar warming of late 2016 and 2019 were primarily manifestations  
377 of internal climate variability. This assessment is in agreement with previous analyses that  
378 examine mechanisms responsible for recent declines in Antarctic SIE (e.g., Stuecker et al.,  
379 2017; Eayrs et al., 2021).

380 Given the spatial extent, timescale, and magnitude of the late 2016 and 2019 circumpo-  
381 lar surface warming anomalies, it is unlikely that these events signify a long-term shift in the  
382 South Ocean climate. As the circumpolar westerlies continue to intensify and shift poleward,  
383 the upper overturning cell of the Southern Ocean is expected to strengthen, increasing the  
384 upwelling of warm Circumpolar Deep Water across the Antarctic sea ice zone (Ferreira et  
385 al., 2015; Kostov et al., 2017). Additionally, stronger winds will likely energize eddies across  
386 the circumpolar channel that will partially negate the Ekman overturning response (Farneti  
387 et al., 2010; Doddridge et al., 2019). However, the warming rates associated with these  
388 adjustments to the Southern Ocean overturning circulation are expected to be orders of  
389 magnitude smaller than the anomalous surface warming observed during the austral spring  
390 of 2016 and 2019. Further, the recent circumpolar surface warming events spanned the  
391 ice-free regions of the Southern Ocean, where potential temperature decreases with depth  
392 below the seasonal pycnocline. However, there is evidence that interannual upper ocean up-  
393 welling trends contributed substantially to the prolonged period of below-average Antarctic  
394 SIE between 2016 and 2020 Meehl et al. (2019). The recent decline in Antarctic sea ice  
395 cover has been most pronounced in the Weddell Sea (Parkinson, 2019), which featured large  
396 open-ocean polynyas and deep convection during the winters of 2016 and 2017 (Cheon &  
397 Gordon, 2019). These polynya events were facilitated by enhanced upwelling across the  
398 Weddell Gyre, which gradually eroded the local pycnocline and preconditioned the region  
399 for deep convection (Campbell et al., 2019). Thus, we surmise that the anomalous Southern  
400 Ocean surface warming and sea ice loss since 2016 were primarily due to a culmination of  
401 several climate processes acting over sub-seasonal to interannual timescales.

402 Additional work is needed to determine how the variability of SAM and its impacts on  
403 Southern Ocean MLD and SST will evolve under anthropogenic forcing. Previous studies  
404 have primarily focused on the mean-state ocean response to the ongoing trend toward a more  
405 positive SAM phase, in particular, the ocean overturning response to a strengthening and  
406 poleward shift of the circumpolar westerlies (e.g., Bitz & Polvani, 2012; Ferreira et al., 2015;  
407 Kostov et al., 2017). However, our results demonstrate that near-surface processes acting  
408 on sub-seasonal timescales will set future surface warming extremes. The current positive  
409 trend in the SAM index is largest in austral summer (Fogt & Marshall, 2020), which favors  
410 more vigorous wind-driven mixing and deeper mixed layers. On the other hand, current  
411 surface warming and freshening trends will induce stronger near-surface stratification and  
412 possibly shallower mixed layers. Over the past several decades, these competing processes  
413 have led to a deepening of the Southern Ocean mixed layer and a concurrent enhancement  
414 of the stratification across the base of the mixed layer (Sallée et al., 2021). The extent to  
415 which these trends persist will impact the frequency and intensity of future abrupt surface  
416 warming events and marine heatwaves in the Southern Ocean.

## 417 **5 Conclusions**

418 The abrupt Southern Ocean surface warming anomalies of late 2016 and 2019 were  
419 primarily the result of amplified air-sea heating and reduced northward Ekman transport.  
420 The former effect was due to an unusually early springtime shoaling of the Southern Ocean  
421 mixed layer. Both surface warming events were initiated by a collapse of the circumpolar  
422 westerlies, associated with extreme negative SAM events. Equivalent climate events are  
423 found in the CESM1-LE, wherein the Southern Ocean SST and MLD response to SAM are  
424 consistent with recent observations. Therefore, it is plausible that recent Southern Ocean  
425 surface warming anomalies arose purely from internal variability. A key takeaway from this  
426 work is that SAM has significant control over the seasonal phasing of MLD shoaling in austral  
427 spring, which modulates the interannual variability of summertime SST across the Southern  
428 Ocean. Further work is required to investigate how smaller-scale processes, ranging from  
429 zonal-wavenumber-three atmospheric anomalies (Raphael, 2004) to sub-mesoscale ocean  
430 dynamics (Su et al., 2018), may augment regional SST variability and produce local MHWs,  
431 as well as how interannual SAM variability and summertime Southern Ocean SST will evolve  
432 during the 21st century.

## 6 Open Research

All data and reanalysis products used in this study are sourced from publicly accessible repositories. NOAA Optimum Interpolation SST V2 data were retrieved from <https://psl.noaa.gov/data/gridded/data.noaa.oisst.v2.html>. The Roemmich-Gilson Argo product was downloaded from <https://sio-argo.ucsd.edu/RG.Climatology.html>. ERA5 reanalysis can be accessed at <https://doi.org/10.24381/cds.f17050d7>. Model output from the CESM1-LE can be downloaded from <https://www.cesm.ucar.edu/projects/community-projects/LENS/data-sets.html>. NOAA/NSIDC Climate Data Record of Passive Microwave Sea Ice Concentration (Version 4) can be accessed at <https://doi.org/10.7265/efmz-2t65z>. Python code for carrying out analysis and generating figures is available at <https://doi.org/10.5281/zenodo.6588645>.

### Acknowledgments

E.A.W. acknowledges support from Caltech's Terrestrial Hazard Observations and Reporting Center. D.B.B. was supported by the National Science Foundation Graduate Research Fellowship Program (NSF Grant DGE-1745301). A.F.T. received support from NSF award OCE-1756956 and the Internal Research and Technology Development program (Earth 2050), Jet Propulsion Laboratory, California Institute of Technology. E.A.W. and S.C.R. received support through the SOCCOM Project, funded by the National Science Foundation, Division of Polar Programs (NSF PLR-1425989 and OPP-1936222). E.A.W. and S.C.R. also received funding from NOAA as part of the US Argo Program via grant NA20OAR4320271 to the University of Washington.

### Conflict of Interest

The authors have no conflicts of interest to declare.

## Appendix A Ensemble experiments with a 1D mixing model

To evaluate the impact of wind perturbations on MLT warming, we use a modified version of the Kraus-Turner 1D upper ocean mixing model (Kraus & Turner, 1967; Niiler, 1975; Niiler & Kraus, 1977). This bulk mixed layer model simulates the evolution of the surface mixed layer by balancing the stabilizing effect of surface buoyancy fluxes (i.e., the addition of heat or freshwater to the water column) and the destabilizing effect of wind-driven mixing. Variants of the Kraus-Turner model have been used extensively to study

463 surface mixed layer variations over a wide range of settings, including in subpolar regions  
 464 (Biddle et al., 2017). Following Chen et al. (1994), the entrainment rate,  $w_{ent}$ , of the mixed  
 465 layer is given by

$$466 \quad w_{ent} = \frac{P_w - P_b}{h_m \Delta b}, \quad (\text{A1})$$

467 where  $\Delta b$  is the buoyancy difference across the base of the mixed layer, and  $P_w$  and  $P_b$  are  
 468 work provided by surface wind stress and the potential energy supplied by surface buoyancy  
 469 fluxes, respectively.  $P_w$  and  $P_b$  are given by

$$470 \quad P_w = 2\gamma_1 u_*^3, \quad (\text{A2})$$

$$471 \quad P_b = \frac{h_m}{2} [(1 + \gamma_2) B_0 - (1 - \gamma_2) |B_0|], \quad (\text{A3})$$

472 where  $\gamma_1 = 0.4$  and  $\gamma_2 = 0.18$  are empirically derived mixing coefficients,  $u_*$  is the friction  
 473 velocity, and  $B_0$  is the total surface buoyancy flux. The above formulation is valid for a  
 474 stably stratified water column ( $\Delta b > 0$ ). For scenarios where  $P_w - P_b > 0$ , the mixed  
 475 layer deepens and (A1) is used to determine the entrainment rate. For cases of mixed layer  
 476 shoaling, we assume  $P_w$  and  $P_b$  are in balance and we use the relationships (A2) and (A3)  
 477 to determine  $h_m$ .  
 478

479 The mixing model is initialized with idealized temperature and salinity profiles repre-  
 480 sentative of the circumpolar channel between 50°–65°S in early October. At the start of  
 481 each simulation, the mixed layer depth is set to 125 m, and temperature and salinity in  
 482 the mixed layer are set to 1 °C and 33.4 PSU, respectively. Below the mixed layer, there  
 483 is a 150 m thick seasonal pycnocline, across which temperature and salinity linearly transi-  
 484 tion to fixed values of 0°C and ~33.6 PSU, respectively. We prescribe a surface heat flux  
 485 that approximates the climatological net surface heating across the circumpolar channel  
 486 between October and March (150 days total). To isolate the impact of surface winds and  
 487 heating, we impose a constant surface freshwater flux (i.e., precipitation minus evaporation)  
 488 of 1 mm day<sup>-1</sup>. The buoyancy forcing is combined with a synthetically generated surface  
 489 wind stress  $\tau$ , which is modeled as the sum of a red-noise sequence  $\hat{\tau}(t)$  and a mean offset  
 490  $\bar{\tau}$ :

$$491 \quad \tau(t) = \hat{\tau}(t) + \bar{\tau}, \quad (\text{A4})$$

$$492 \quad \hat{\tau}(t) = a \hat{\tau}(t - \Delta t) + \sqrt{(1 - a^2)} \epsilon(t), \quad (\text{A5})$$

493 where  $a = 0.9$  is the lag-1 auto-correlation coefficient,  $\Delta t = 6$  hours is the time step,  $\epsilon$   
 494 is a randomly generated white noise sequence with a standard deviation of 0.05, and  $\bar{\tau}$   
 495

496 = 0.1 N m<sup>-2</sup>. The numerical model is evolved with a vertical resolution of 0.25 m and  
 497 a 6 hourly time step. A total of six ensemble experiments are carried out: one control  
 498 experiment consisting of 200 independent simulations, each with a unique wind forcing, and  
 499 five perturbation experiments wherein  $\bar{\tau}$  is reduced over different time windows, centered  
 500 on days 15, 45, 75, 105, and 135 days (after October 1). For the perturbation experiments,  
 501 the magnitude of the time-mean wind stress is reduced by a maximum of 50% using a  
 502 Gaussian window with a standard deviation of 5 days. By perturbing  $\bar{\tau}$  in Equation (A5),  
 503 the temporal variance of  $\tau$  is preserved.

## 504 References

- 505 Armour, K. C., Marshall, J., Scott, J. R., Donohoe, A., & Newsom, E. R. (2016). Southern  
 506 Ocean warming delayed by circumpolar upwelling and equatorward transport. *Nat.*  
 507 *Geosci.*, *9*(7), 549–554. doi: <https://doi.org/10.1038/ngeo2731>
- 508 Biddle, L. C., Heywood, K. J., Kaiser, J., & Jenkins, A. (2017). Glacial meltwater  
 509 identification in the Amundsen Sea. *J. Phys. Oceanogr.*, JPO–D–16–0221.1. doi:  
 510 <https://doi.org/10.1175/JPO-D-16-0221.1>
- 511 Bintanja, R., Van Oldenborgh, G. J., Drijfhout, S. S., Wouters, B., & Katsman, C. A. (2013).  
 512 Important role for ocean warming and increased ice-shelf melt in Antarctic sea-ice  
 513 expansion. *Nat. Geosci.*, *6*(5), 376–379. doi: <https://doi.org/10.1038/ngeo1767>
- 514 Bitz, C. M., & Polvani, L. M. (2012). Antarctic climate response to stratospheric ozone  
 515 depletion in a fine resolution ocean climate model. *Geophys. Res. Lett.*, *39*(20). doi:  
 516 <https://doi.org/10.1029/2012GL053393>
- 517 Campbell, E. C., Wilson, E. A., Moore, G. W., Riser, S. C., Brayton, C. E., Mazloff, M. R.,  
 518 & Talley, L. D. (2019). Antarctic offshore polynyas linked to Southern Hemisphere  
 519 climate anomalies. *Nature*, *570*(7761), 319–325. doi: <https://doi.org/10.1038/s41586-019-1294-0>
- 520
- 521 Carranza, M. M., & Gille, S. T. (2015). Southern Ocean wind-driven entrainment enhances  
 522 satellite chlorophyll-a through the summer. *J. Geophys. Res. Ocean.*, *120*(1), 304–323.  
 523 doi: <https://doi.org/10.1002/2014JC010203>
- 524 Cavalieri, D. J., Parkinson, C. L., & Vinnikov, K. Y. (2003). 30-year satellite record  
 525 reveals contrasting Arctic and Antarctic decadal sea ice variability. *Geophys. Res.*  
 526 *Lett.*, *30*(18). doi: <https://doi.org/10.1029/2003GL018031>
- 527 Chen, D., Rothstein, L. M., & Busalacchi, A. J. (1994). A Hybrid Vertical Mixing Scheme

- 528 and Its Application to Tropical Ocean Models. *J. Phys. Oceanogr.*, *24*(10), 2156–2179.  
529 doi: [https://doi.org/10.1175/1520-0485\(1994\)024<2156:AHVMSA>2.0.CO;2](https://doi.org/10.1175/1520-0485(1994)024<2156:AHVMSA>2.0.CO;2)
- 530 Cheon, W. G., & Gordon, A. L. (2019). Open-ocean polynyas and deep convection in  
531 the Southern Ocean. *Sci. Rep.*, *9*(1), 6935. doi: <https://doi.org/10.1038/s41598-019-43466-2>
- 532
- 533 Chung, E.-S., Kim, S.-J., Timmermann, A., Ha, K.-J., Lee, S.-K., Stuecker, M. F., ...  
534 Huang, L. (2022). Antarctic sea-ice expansion and Southern Ocean cooling linked  
535 to tropical variability. *Nat. Clim. Chang.*. doi: <https://doi.org/10.1038/s41558-022-01339-z>
- 536
- 537 Ciasto, L. M., & England, M. H. (2011). Observed ENSO teleconnections to Southern  
538 Ocean SST anomalies diagnosed from a surface mixed layer heat budget. *Geophys.*  
539 *Res. Lett.*, *38*(9). doi: <https://doi.org/10.1029/2011GL046895>
- 540 de Boyer Montégut, C., Madec, G., Fischer, A. S., Lazar, A., & Iudicone, D. (2004). Mixed  
541 layer depth over the global ocean: An examination of profile data and a profile-based  
542 climatology. *J. Geophys. Res. C Ocean.*, *109*(12), 1–20. doi: <https://doi.org/10.1029/2004JC002378>
- 543
- 544 Ding, Q., Steig, E. J., Battisti, D. S., & Wallace, J. M. (2012). Influence of the tropics  
545 on the southern annular mode. *J. Clim.*, *25*(18), 6330–6348. doi: <https://doi.org/10.1175/JCLI-D-11-00523.1>
- 546
- 547 Doddridge, E. W., Marshall, J., Song, H., Campin, J. M., Kelley, M., & Nazarenko, L.  
548 (2019). Eddy Compensation Dampens Southern Ocean Sea Surface Temperature  
549 Response to Westerly Wind Trends. *Geophys. Res. Lett.*, *46*(8), 4365–4377. doi:  
550 <https://doi.org/10.1029/2019GL082758>
- 551 Dong, S., Gille, S. T., & Sprintall, J. (2007). An assessment of the Southern Ocean  
552 mixed layer heat budget. *J. Clim.*, *20*(17), 4425–4442. doi: <https://doi.org/10.1175/JCLI4259.1>
- 553
- 554 Dong, S., Sprintall, J., Gille, S. T., & Talley, L. (2008). Southern ocean mixed-layer depth  
555 from Argo float profiles. *J. Geophys. Res. Ocean.*, *113*(6). doi: <https://doi.org/10.1029/2006JC004051>
- 556
- 557 du Plessis, M., Swart, S., Biddle, L. C., Giddy, I. S., Monteiro, P. M. S., Reason, C. J. C.,  
558 ... Nicholson, S. (2022). The Daily-Resolved Southern Ocean Mixed Layer: Regional  
559 Contrasts Assessed Using Glider Observations. *J. Geophys. Res. Ocean.*, *127*(4). doi:  
560 <https://doi.org/10.1029/2021JC017760>

- 561 Eyras, C., Li, X., Raphael, M. N., & Holland, D. M. (2021). Rapid decline in Antarctic  
562 sea ice in recent years hints at future change. *Nat. Geosci.*, *14*(7), 460–464. doi:  
563 <https://doi.org/10.1038/s41561-021-00768-3>
- 564 Fan, T., Deser, C., & Schneider, D. P. (2014). Recent Antarctic sea ice trends in the context  
565 of Southern Ocean surface climate variations since 1950. *Geophys. Res. Lett.*, *41*(7),  
566 2419–2426. doi: <https://doi.org/10.1002/2014GL059239>
- 567 Farneti, R., Delworth, T. L., Rosati, A. J., Griffies, S. M., & Zeng, F. (2010). The role of  
568 mesoscale eddies in the rectification of the Southern ocean response to climate change.  
569 *J. Phys. Oceanogr.*, *40*(7), 1539–1557. doi: <https://doi.org/10.1175/2010JPO4353.1>
- 570 Ferreira, D., Marshall, J., Bitz, C. M., Solomon, S., & Plumb, A. (2015). Antarctic ocean  
571 and sea ice response to ozone depletion: A two-time-scale problem. *J. Clim.*, *28*(3),  
572 1206–1226. doi: <https://doi.org/10.1175/JCLI-D-14-00313.1>
- 573 Fogt, R. L., & Marshall, G. J. (2020). The Southern Annular Mode: Variability, trends,  
574 and climate impacts across the Southern Hemisphere. *WIREs Clim. Chang.*, *11*(4).  
575 doi: <https://doi.org/10.1002/wcc.652>
- 576 Frölicher, T. L., Fischer, E. M., & Gruber, N. (2018). Marine heatwaves under global  
577 warming. *Nature*, *560*(7718), 360–364. doi: <https://doi.org/10.1038/s41586-018-0383>  
578 -9
- 579 Gao, Y., Kamenkovich, I., Perlin, N., & Kirtman, B. (2022). Oceanic Advection Controls  
580 Mesoscale Mixed Layer Heat Budget and Air–Sea Heat Exchange in the Southern  
581 Ocean. *J. Phys. Oceanogr.*, *52*(4), 537–555. doi: <https://doi.org/10.1175/JPO-D-21>  
582 -0063.1
- 583 Haumann, F. A., Gruber, N., & Münnich, M. (2020). Sea-Ice Induced Southern Ocean  
584 Subsurface Warming and Surface Cooling in a Warming Climate. *AGU Adv.*, *1*(2).  
585 doi: <https://doi.org/10.1029/2019AV000132>
- 586 Hersbach, H., Bell, B., Berrisford, P., Hirahara, S., Horányi, A., Muñoz-Sabater, J., ...  
587 Thépaut, J. N. (2020). The ERA5 global reanalysis. *Q. J. R. Meteorol. Soc.*, *146*(730),  
588 1999–2049. doi: <https://doi.org/10.1002/qj.3803>
- 589 Hobday, A. J., Alexander, L. V., Perkins, S. E., Smale, D. A., Straub, S. C., Oliver, E. C.,  
590 ... Wernberg, T. (2016). A hierarchical approach to defining marine heatwaves. *Prog.*  
591 *Oceanogr.*, *141*, 227–238. doi: <https://doi.org/10.1016/j.pocean.2015.12.014>
- 592 Holbrook, N. J., Scannell, H. A., Sen Gupta, A., Benthuisen, J. A., Feng, M., Oliver, E. C.,  
593 ... Wernberg, T. (2019). A global assessment of marine heatwaves and their drivers.

- 594 *Nat. Commun.*, 10(1), 2624. doi: <https://doi.org/10.1038/s41467-019-10206-z>
- 595 Kay, J. E., Deser, C., Phillips, A., Mai, A., Hannay, C., Strand, G., ... Vertenstein, M.  
596 (2015). The Community Earth System Model (CESM) Large Ensemble Project: A  
597 Community Resource for Studying Climate Change in the Presence of Internal Climate  
598 Variability. *Bull. Am. Meteorol. Soc.*, 96(8), 1333–1349. doi: [https://doi.org/10.1175/  
599 BAMS-D-13-00255.1](https://doi.org/10.1175/BAMS-D-13-00255.1)
- 600 Kostov, Y., Marshall, J., Hausmann, U., Armour, K. C., Ferreira, D., & Holland, M. M.  
601 (2017). Fast and slow responses of Southern Ocean sea surface temperature to SAM  
602 in coupled climate models. *Clim. Dyn.*, 48(5-6), 1595–1609. doi: [https://doi.org/  
603 10.1007/s00382-016-3162-z](https://doi.org/10.1007/s00382-016-3162-z)
- 604 Kraus, E. B., & Turner, J. S. (1967). A one-dimensional model of the seasonal thermocline  
605 II. The general theory and its consequences. *Tellus*, 19(1), 98–106. doi: [https://  
606 doi.org/10.3402/tellusa.v19i1.9753](https://doi.org/10.3402/tellusa.v19i1.9753)
- 607 Li, X., Cai, W., Meehl, G. A., Chen, D., Yuan, X., Raphael, M., ... Song, C. (2021). Tropical  
608 teleconnection impacts on Antarctic climate changes. *Nat. Rev. Earth Environ.*, 2(10),  
609 680–698. doi: <https://doi.org/10.1038/s43017-021-00204-5>
- 610 Marshall, G. J. (2003). Trends in the Southern Annular Mode from observations and re-  
611 analyses. *J. Clim.*, 16(24), 4134–4143. doi: [https://doi.org/10.1175/1520-0442\(2003\)  
612 016<4134:TITSAM>2.0.CO;2](https://doi.org/10.1175/1520-0442(2003)016<4134:TITSAM>2.0.CO;2)
- 613 Meehl, G. A., Arblaster, J. M., Bitz, C. M., Chung, C. T., & Teng, H. (2016). Antarctic  
614 sea-ice expansion between 2000 and 2014 driven by tropical Pacific decadal climate  
615 variability. *Nat. Geosci.*, 9(8), 590–595. doi: <https://doi.org/10.1038/ngeo2751>
- 616 Meehl, G. A., Arblaster, J. M., Chung, C. T., Holland, M. M., DuVivier, A., Thompson,  
617 L. A., ... Bitz, C. M. (2019). Sustained ocean changes contributed to sudden Antarctic  
618 sea ice retreat in late 2016. *Nat. Commun.*, 10(1). doi: [https://doi.org/10.1038/  
619 s41467-018-07865-9](https://doi.org/10.1038/s41467-018-07865-9)
- 620 Meier, W., Fetterer, F., Savoie, M., Mallory, S., Duerr, R., & Stroeve, J. (2013).  
621 *NOAA/NSIDC Climate Data Record of Passive Microwave Sea Ice Concentration*.  
622 Boulder, Colorado USA.: NSIDC: National Snow and Ice Data Center. doi: [https://  
623 doi.org/10.7265/N59P2ZTG](https://doi.org/10.7265/N59P2ZTG)
- 624 Niiler, P. P. (1975). The deepening of the wind-mixed layer. *J. Mar. Res.*, 33(3), 405—422.
- 625 Niiler, P. P., & Kraus, E. B. (1977). One Dimensional Models of the Upper Ocean. In  
626 E. B. Kraus (Ed.), *Model. predict. up. layers ocean* (pp. 143—172). New York: Perg-

- 627 amon.
- 628 Oliver, E. C., Benthuisen, J. A., Darmaraki, S., Donat, M. G., Hobday, A. J., Holbrook,  
629 N. J., ... Sen Gupta, A. (2021). Marine Heatwaves. *Ann. Rev. Mar. Sci.*, *13*(1),  
630 313–342. doi: <https://doi.org/10.1146/annurev-marine-032720-095144>
- 631 Parkinson, C. L. (2019). A 40-y record reveals gradual Antarctic sea ice increases followed  
632 by decreases at rates far exceeding the rates seen in the Arctic. *Proc. Natl. Acad. Sci.*,  
633 *116*(29), 14414–14423. doi: <https://doi.org/10.1073/pnas.1906556116>
- 634 Pellichero, V., Sallée, J. B., Schmidtko, S., Roquet, F., & Charrassin, J. B. (2017). The ocean  
635 mixed layer under Southern Ocean sea-ice: Seasonal cycle and forcing. *J. Geophys.*  
636 *Res. Ocean.*, *122*(2), 1608–1633. doi: <https://doi.org/10.1002/2016JC011970>
- 637 Purich, A., & England, M. H. (2019). Tropical Teleconnections to Antarctic Sea Ice During  
638 Austral Spring 2016 in Coupled Pacemaker Experiments. *Geophys. Res. Lett.*, *46*(12),  
639 6848–6858. doi: <https://doi.org/10.1029/2019GL082671>
- 640 Purich, A., England, M. H., Cai, W., Sullivan, A., & Durack, P. J. (2018). Impacts of  
641 broad-scale surface freshening of the Southern Ocean in a coupled climate model. *J.*  
642 *Clim.*, *31*(7), 2613–2632. doi: <https://doi.org/10.1175/JCLI-D-17-0092.1>
- 643 Rackow, T., Danilov, S., Goessling, H. F., Hellmer, H. H., Sein, D. V., Semmler, T., ...  
644 Jung, T. (2022). Delayed Antarctic sea-ice decline in high-resolution climate change  
645 simulations. *Nat. Commun.*, *13*(1), 637. doi: <https://doi.org/10.1038/s41467-022-28259-y>
- 646
- 647 Raphael, M. N. (2004). A zonal wave 3 index for the Southern Hemisphere. *Geophys. Res.*  
648 *Lett.*, *31*(23). doi: <https://doi.org/10.1029/2004GL020365>
- 649 Reynolds, R. W., Rayner, N. A., Smith, T. M., Stokes, D. C., & Wang, W. (2002). An  
650 improved in situ and satellite SST analysis for climate. *J. Clim.*, *15*(13), 1609–1625.  
651 doi: [https://doi.org/10.1175/1520-0442\(2002\)015<1609:AIISAS>2.0.CO;2](https://doi.org/10.1175/1520-0442(2002)015<1609:AIISAS>2.0.CO;2)
- 652 Roemmich, D., & Gilson, J. (2009). The 2004–2008 mean and annual cycle of temperature,  
653 salinity, and steric height in the global ocean from the Argo Program. *Prog. Oceanogr.*,  
654 *82*(2), 81–100. doi: <https://doi.org/10.1016/j.pocean.2009.03.004>
- 655 Sallée, J.-B., Pellichero, V., Akhoudas, C., Pauthenet, E., Vignes, L., Schmidtko, S., ...  
656 Kuusela, M. (2021). Summertime increases in upper-ocean stratification and mixed-  
657 layer depth. *Nature*, *591*(7851), 592–598. doi: <https://doi.org/10.1038/s41586-021-03303-x>
- 658
- 659 Sallée, J. B., Speer, K. G., & Rintoul, S. R. (2010). Zonally asymmetric response of the

- 660 Southern Ocean mixed-layer depth to the Southern Annular Mode. *Nat. Geosci.*, *3*(4),  
 661 273–279. doi: <https://doi.org/10.1038/ngeo812>
- 662 Schlosser, E., Alexander Haumann, F., & Raphael, M. N. (2018). Atmospheric influences  
 663 on the anomalous 2016 Antarctic sea ice decay. *Cryosphere*, *12*(3), 1103–1119. doi:  
 664 <https://doi.org/10.5194/tc-12-1103-2018>
- 665 Sen Gupta, A., & England, M. H. (2006). Coupled ocean-atmosphere-ice response to  
 666 variations in the southern annular mode. *J. Clim.*, *19*(18), 4457–4486. doi: <https://doi.org/10.1175/JCLI3843.1>
- 667  
 668 Simmonds, I. (2015). Comparing and contrasting the behaviour of Arctic and Antarctic  
 669 sea ice over the 35 year period 1979-2013. *Ann. Glaciol.*, *56*(69), 18–28. doi: <https://doi.org/10.3189/2015AoG69A909>
- 670  
 671 Smale, D. A., Wernberg, T., Oliver, E. C., Thomsen, M., Harvey, B. P., Straub, S. C., ...  
 672 Moore, P. J. (2019). Marine heatwaves threaten global biodiversity and the provision  
 673 of ecosystem services. *Nat. Clim. Chang.*, *9*(4), 306–312. doi: <https://doi.org/10.1038/s41558-019-0412-1>
- 674  
 675 Stuecker, M. F., Bitz, C. M., & Armour, K. C. (2017). Conditions leading to the unprece-  
 676 dented low Antarctic sea ice extent during the 2016 austral spring season. *Geophys.  
 677 Res. Lett.*, *44*(17), 9008–9019. doi: <https://doi.org/10.1002/2017GL074691>
- 678 Su, Z., Wang, J., Klein, P., Thompson, A. F., & Menemenlis, D. (2018). Ocean subme-  
 679 soscales as a key component of the global heat budget. *Nat. Commun.*, *9*(1), 775. doi:  
 680 <https://doi.org/10.1038/s41467-018-02983-w>
- 681 Tamsitt, V., Talley, L. D., Mazloff, M. R., & Cerovecki, I. (2016). Zonal variations in  
 682 the Southern Ocean heat budget. *J. Clim.*, *29*(18), 6563–6579. doi: <https://doi.org/10.1175/JCLI-D-15-0630.1>
- 683  
 684 Turner, J., Phillips, T., Marshall, G. J., Hosking, J. S., Pope, J. O., Bracegirdle, T. J.,  
 685 & Deb, P. (2017). Unprecedented springtime retreat of Antarctic sea ice in 2016.  
 686 *Geophys. Res. Lett.*, *44*(13), 6868–6875. doi: <https://doi.org/10.1002/2017GL073656>
- 687 Wang, G., Hendon, H. H., Arblaster, J. M., Lim, E. P., Abhik, S., & van Rensch, P. (2019).  
 688 Compounding tropical and stratospheric forcing of the record low Antarctic sea-ice in  
 689 2016. *Nat. Commun.*, *10*(1), 13. doi: <https://doi.org/10.1038/s41467-018-07689-7>
- 690 Yuan, X., & Martinson, D. G. (2000). Antarctic sea ice extent variability and its  
 691 global connectivity. *J. Clim.*, *13*(10), 1697–1717. doi: [https://doi.org/10.1175/1520-0442\(2000\)013\(1697:ASIEVA\)2.0.CO;2](https://doi.org/10.1175/1520-0442(2000)013(1697:ASIEVA)2.0.CO;2)
- 692

693 Zhang, L., Delworth, T. L., Cooke, W., & Yang, X. (2019). Natural variability of Southern  
694 Ocean convection as a driver of observed climate trends. *Nat. Clim. Chang.*, *9*(1),  
695 59–65. doi: <https://doi.org/10.1038/s41558-018-0350-3>